Scaling in kth-passage percolation

Miguel Gómez Donoso*

Universidad Nacional de Educación a Distancia (UNED)

(Dated: July 2, 2021)

Abstract

The kth-passage percolation model is proposed as a generalization of the first-passage percolation model. Specific samples of k shortest simple paths in random square lattices are analyzed, revealing a potentially ultrametric structure in the overlaps between paths. The average scaling behaviour of the arrival time and its fluctuations is calculated, providing evidence that the usual Kardar–Parisi–Zhang universality class for interface growth is attained after a pre-asymptotic regime whose extent increases with k.

Keywords: percolation problems, fluctuation phenomena, interfaces in random media

CONTENTS

I. Motivation and purpose 4

II. Background 6

A. Equilibrium systems: the Lenz–Ising ferromagnet 7

1. Universality 7

2. Renormalisation 8

3. Scaling 9

4. Thermodynamic limit and ergodicity 10

B. Out-of-equilibrium systems: the Sherrington-Kirkpatrick spin glass 10

1. Replica trick and overlap 12

2. Replica-symmetric solution 13

3. Replica symmetry breaking 14

4. Ultrametricity 15

C. Non-equilibrium systems: surface growth in first-passage percolation 17

1. Kardar–Parisi–Zhang universality class 18

2. First-passage percolation model 19

D. The k shortest simple paths problem 21

1. Shortest path 21

2. Ranking shortest paths 23

* Supervisors: Javier Rodríguez-Laguna and Pedro Córdoba-Torres; miguelgdonoso@gmail.com

III. Methodology 26
A. Parameter variables 26
B. Shortest paths algorithm 27
C. Overlaps and dendrograms 27

IV. Results and discussion 28
A. Samples 28
B. Average overlaps 31
C. Average minimal arrival time fluctuations 33

V. Conclusions and future work 35

Acknowledgments 36

References 36

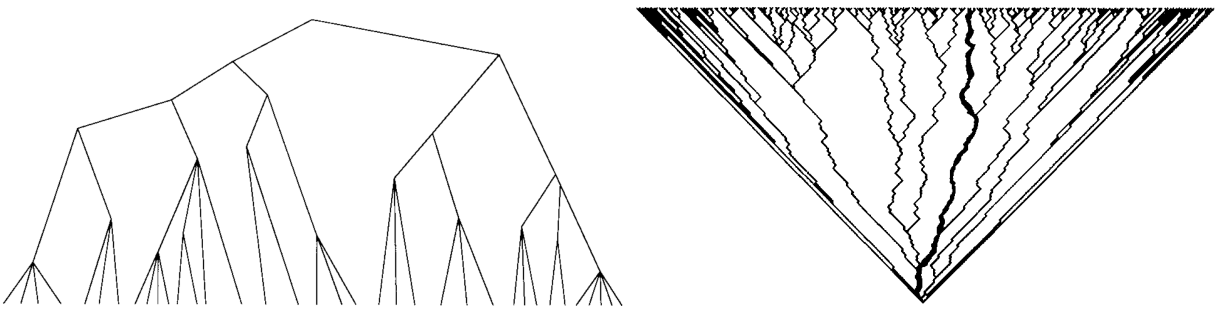

FIG. 1: Left: Sketch of the hierarchical structure of spin glass states, which correspond to the leaves at the bottom. The more similar the states, the lower they branch. From [1]. Right: Locally optimal paths in a realization of a DPRM surface growth model. From [2].

I. MOTIVATION AND PURPOSE

This work has two main ingredients: the fractal-like nature of surface growth and the hierarchical structure of amorphous solids.

The irregular nature of amorphous solids is often modelled as spin systems with random couplings, known as spin glasses. The chief consequence of this randomness is their characteristically rough energy landscape and its myriad valleys (local minima). These are theoretically best explained by Parisi's replica-symmetry breaking, which revealed the hierarchical structure of the valleys, commonly referred to as *ultrametric* (left side of figure 1).

On the other hand, one of the best-known growth models is the first-passage percolation (FPP) model, which describes the single-source spread of geodesics in random graphs. These and other surface growth models have, in recent decades, drawn significant attention to their scaling behaviour, often described by the Kardar–Parisi–Zhang (KPZ) universality class (figures 2 and 3).

Additionally, the FPP model resembles many natural phenomena such as stains, fire fronts, and surfaces of growing crystals. The latter is showcased in figure 2, along with FPP model samples of an interface and some geodesics, which also display a hierarchical fractal-like structure. Another instance of a hierarchy in a growth model can be found in the directed polymers in random media (DPRM) model (right side of figure 1).

The presence of these hierarchies in both classes of systems invites further thought on the nature of these hierarchies. Given that the ultrametric structure of spin glasses is well established, it is used in this work to propose and probe a generalisation of the FPP model.

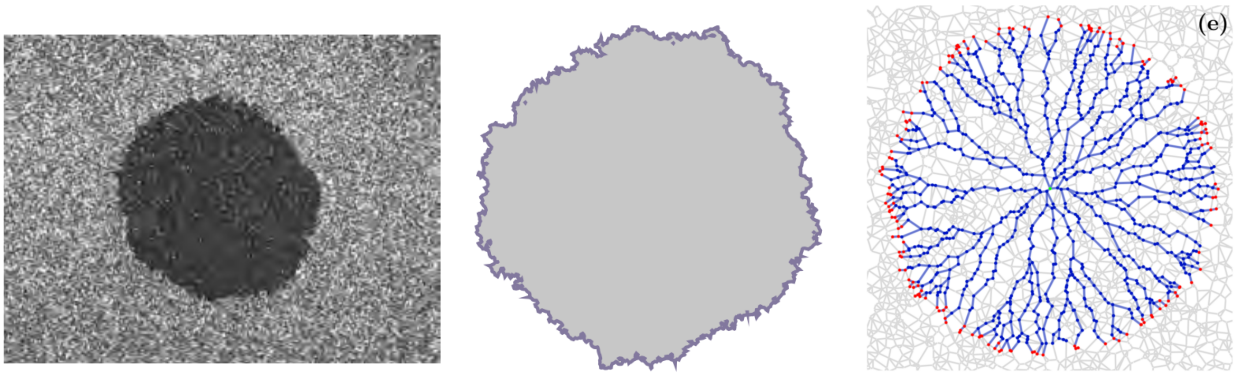

FIG. 2: Left: Interface in liquid-crystal turbulence whose growth follows KPZ. From [3]. Centre: A realization of an FPP growth model on a random geometry. From [3]. Right: The geodesics of another FPP model reveal a hierarchical structure. From [4].

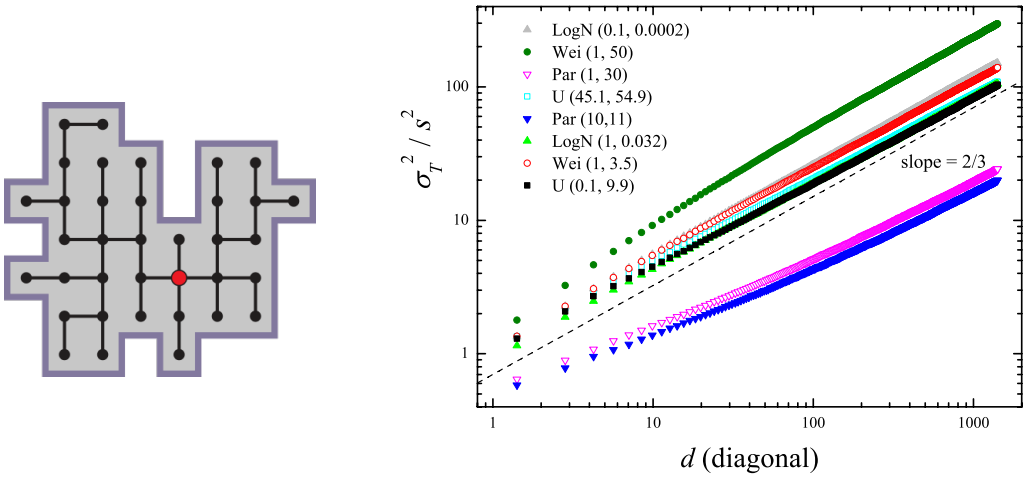

FIG. 3: FPP model on a square lattice. Left: Growing cluster. From [3]. Right: KPZ scaling of the arrival time fluctuations along the diagonal of the lattice. From [5].

While the FPP model is fully defined by its geodesics (i.e., shortest paths), the complex energy landscape of a spin glass is determined by its complete set of local minima, not just its global one. This comparison suggests a generalization of FPP models whose geometry is induced not by shortest paths (minimal arrival times) but instead by k shortest paths.

Indeed, the main purpose of this work is to probe the structure and scaling behaviour of the proposed kth-passage percolation (KPP) model in square lattices. Of particular interest is whether 1) the sets of k-shortest paths have an ultrametric structure and 2) their scaling behaviour is described by KPZ.

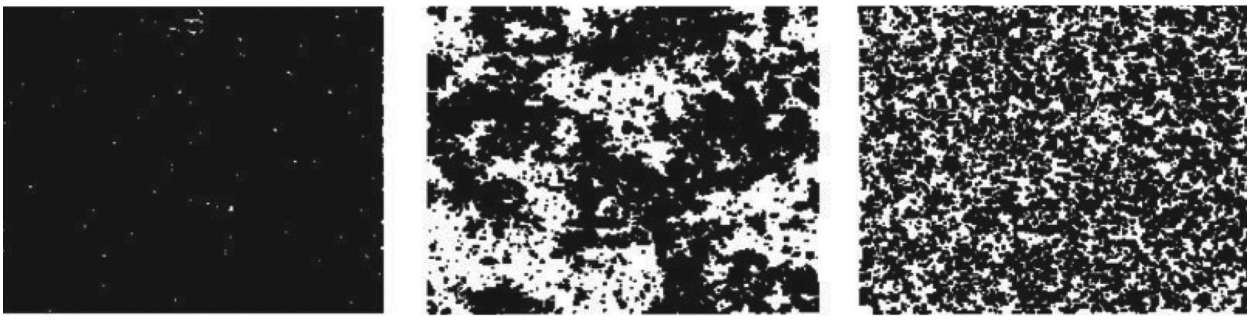

FIG. 4: Two-dimensional zero-field Lenz-Ising model. Left: subcritical temperature. Centre: critical temperature. Right: supercritical temperature. From [6].

II. BACKGROUND

This section is arranged as follows:

a. Equilibrium systems Given that spin glasses and surface growth are non-equilibrium phenomena, the core concept of universal scaling is explained (for completeness and convenience) in the context of a well-known equilibrium system: the Lenz–Ising ferromagnet.

b. Out-of-equilibrium systems These are systems for which equilibrium is defined by a Hamiltonian, but they have been driven out of it or are unable to reach it somehow. In the case of spin glasses, they are unable to reach equilibrium due to the non-ergodic energy landscape that frustration produces. The key concept, ultrametricity, is explained through Sherrington-Kirkpatrick spin glass model.

c. Non-equilibrium systems This is a very broad category covering many types of systems, one of which is surface growth models. The key concept, KPZ scaling, is explained, as well as the first-passage percolation model.

At the end of the section, and disconnected from the previous schema, the problem of ranking shortest paths is discussed, as it is naturally required for the generalization from first-passage percolation to kth-passage percolation.

A. Equilibrium systems: the Lenz–Ising ferromagnet

The Lenz–Ising model [7] consists of a d-dimensional hypercubic grid with $N = L^d$ spins of value $s_i = \pm 1$ and Hamiltonian

$$\mathcal{H} = -J \sum_{i<j} s_i s_j - h \sum_i s_i \,, \tag{1}$$

where J is the spin coupling and h an external field. Additionally, the system is thermodynamically closed and kept at fixed coldness $\beta = 1/k_B T$. Its equilibrium is therefore described by the canonical ensemble, whose averages

$$\langle A \rangle = Z^{-1} \operatorname{Tr} A e^{-\beta \mathcal{H}} \tag{2}$$

can be derived from the partition function $Z = \operatorname{Tr} e^{-\beta \mathcal{H}}$. Figure 4 shows snapshots of the system at different temperatures.

1. Universality

Universality is the observation that large, complex systems with significantly different finite-scale features may share the same scaling behaviour as they tend to a common scale-invariant limit, in which case they belong to the same universality class. This allows one to make testable predictions of a little-understood system using a well-known member of its (assumed) universality class, as is done in §III.

Informally, a scale-invariant object "looks the same at all length scales", which for a function $f(x)$ means that a rescaling of its variable $x \mapsto \ell x$ simply rescales the function without changing its shape, that is,

$$f(\ell x) = \ell^\Delta f(x) \tag{3}$$

and thus $f(x) = x^\Delta$ is a power law. For instance, a scale-invariant limit of the celebrated Lenz-Ising ferromagnet [7] is its critical fixed point, where the configuration of spins is fractal-like and the distribution of cluster sizes follows a power law (figure 4).

Why scale invariance? Because it implies that any relevant physics must survive a rescaling of any size; therefore, only infinite-range features are relevant, such as symmetries or dimensionality. Paradoxically, scale invariance also implies that there is no separation of

scales: all scales coexist and interact and, in particular, fluctuations occur at all length scales. Universality thus seems contradictory: the same scale invariance that makes fluctuations macroscopically relevant also constitutes an emergent symmetry that renders finite-range physics irrelevant and, in doing so, universalises the behaviour of the system. In this sense, universality is the observation that there are relatively few scale-invariant theories.

Fluctuations were—perhaps not coincidentally—one of the early fundamental obstacles that was faced in the historical development of universality. The concept originated in the study of systems at equilibrium undergoing phase transitions (ferromagnets and liquid-gas systems) which produced the classical theories of Van der Vaals and Weiss, eventually leading to the Landau theory of phase transitions [8]. These were all mean-field theories, that is, they ignored fluctuations and thus did not incorporate scaling correctly [9, 10]. In particular, they were unable to explain critical scaling exponents that seemed inconsistent with elementary dimensional analysis (it was later figured out that microscopic length scales has to be taken into account to make it consistent) [11, §7.2].

2. Renormalisation

The first step towards solving this anomaly, put forward by Kadanoff in 1966, was the "block-spin" renormalisation [12], later refined by Wilson in a series of seminal papers [13–15] between 1971 and 1972 that earned him the Nobel prize in 1982. In them, he developed and explained the modern renormalisation group (RG) in the contexts of both condensed matter physics and high energy physics (where renormalisation had been first used to make sense of infinite integrals in the perturbation theory of quantum electrodynamics).

The essence of RG transformations may easily be conveyed in terms of an iterated version of equation (3),

$$f_{n+1}(x) = \ell^{-\Delta} f_n(\ell x) \qquad \text{for} \quad \ell > 1\,, \tag{4}$$

which proceeds in two steps: 1) a dilation $\ell > 1$ of the variable, followed by 2) a contraction $\ell^{-\Delta} < 1$ of the function. The fixed points of this transformation will, by definition (3), be scale-invariant.

Analogously, a (real-space) RG transformation R_ℓ of a d-dimensional system consists of two steps: 1) a coarse-graining transformation that projects the N local degrees of freedom into a new, smaller set of $N' = \ell^{-d} N$ degrees of freedom (while preserving system symme-

tries) [11, p. 238], followed by 2) a contraction ℓ^{-1} of all lengths. The parameters μ of the model thus transform as

$$\mu' = R_\ell(\mu) \qquad \text{for} \quad \ell > 1\,. \tag{5}$$

The set of these transformations together with the operation $R_\ell \circ R_{\ell'} = R_{\ell\ell'}$ defines an abelian semigroup known as the RG, which induces a flow in the parameter space

$$\mu \mapsto R_\ell(\mu) \mapsto R_\ell^2(\mu) \mapsto \cdots \mapsto R_\ell^n(\mu) \mapsto \cdots \tag{6}$$

whose fixed points $\mu^* = R_\ell(\mu^*)$ correspond to scale-invariant theories, that is, universality classes.

At each iteration of R_ℓ, the characteristic length ξ of the system is mapped to $\xi' = \ell^{-1}\xi$, whose only fixed point solutions are either trivial $\xi = 0$ or critical $\xi = \infty$. For other points, $\ell^{-n}\xi \to 0$ as $n \to \infty$, that is, almost all RG flows drive the system away from criticality, eventually converging to trivial fixed points, which are scale-invariant by being homogeneous (and thus correspond to bulk phases, such as the left and right sides of figure 4).

Contrarily, critical fixed points are scale-invariant by being fractal-like (centre of figure 4) and their basin of attraction—known as the critical manifold—is necessarily composed of critical points. Further, the linearised RG transformation $\partial_\mu R_\ell$ at a critical fixed point μ^* must have at least one eigenvalue $\lambda_\ell \geq 1$ (otherwise it would be stable and thus trivial).

In conclusion, a universality class can be characterised by the set of relevant ($\lambda_\ell > 1$) and marginal ($\lambda_\ell = 1$) eigenvalues of its associated fixed point in the RG flow. Irrelevant eigenvalues ($\lambda_\ell < 1$) are only relevant for finite-size effects.

3. Scaling

Wilson's RG was also able to explain the scaling laws first arrived at on a phenomenological basis by Widom [16, 17]. From the semigroup property of the RG it follows that, similarly to equation (3), the eigenvalues must be power laws:

$$\lambda_\ell\,\lambda_{\ell'} = \lambda_{\ell\ell'} \quad \Rightarrow \quad \lambda_\ell^n = \lambda_{\ell^n} \quad \Rightarrow \quad \lambda_\ell = \ell^y\,, \tag{7}$$

where y is a critical scaling exponent. The set of critical exponents associated to a fixed point also characterise a universality class.

4. Thermodynamic limit and ergodicity

In the preceding sections the number N of degrees of freedom was large, but finite. Rigorous scale-invariance demands that the system be in the thermodynamic limit $N \to \infty$ which, in turn, is also necessary for the behaviour at the critical points to be non-analytical.

Perhaps more importantly, in the thermodynamic limit ergodicity might be spontaneously broken along the symmetries of the system, which demands that ensemble averages be restricted to a subset of configuration space. For instance, the Ising model will, under the critical temperature, forever adopt one of two signs ($\pm$) for the average magnetisation. This is not the case for finite N, where finite fluctuations will eventually allow the system to adopt all configurations.

Finally, it is worth noting that all two-dimensional universality classes (with reflection positivity) have been mathematically classified, like elements in a periodic table. This was achieved through a correspondence between two-dimensional universality classes, conformal field theories, and unitary representations of the Virasoro algebra [9, §11.4–5]. This depth of understanding has not been reached for the non-equilibrium systems which now follow.

B. Out-of-equilibrium systems: the Sherrington-Kirkpatrick spin glass

Spin glass models are typically built by introducing random, individual coupling constants J_{ij} in the Lenz–Ising Hamiltonian (1), which may have a physical origin, for example, in the random positions of molecules in an amorphous crystal. This randomness might lead to spins experiencing *frustration*, that is, the incapability of simultaneously satisfying all their couplings due to the coexistence of ferromagnetic and antiferromagnetic patterns.

Frustration, in turn, gives raise to a valley of metastable states in the spin glass phase (figure 5) which completely break ergodicity in the thermodynamic limit. Thus, the system is restricted to one of the valleys, unable to reach equilibrium.

Due to the introduction of the random fields J_{ij}, it is necessary to distinguish Boltzmann–Gibbs ensemble averages $\langle A \rangle$, defined in equation (2), and disorder averages $[A]$ over configurations, given in terms of the probability density $\rho(J_{ij})$ by

$$[A] = \int \prod_{i<j} \mathrm{d}J_{ij}\, \rho(J_{ij})\, A\,. \tag{8}$$

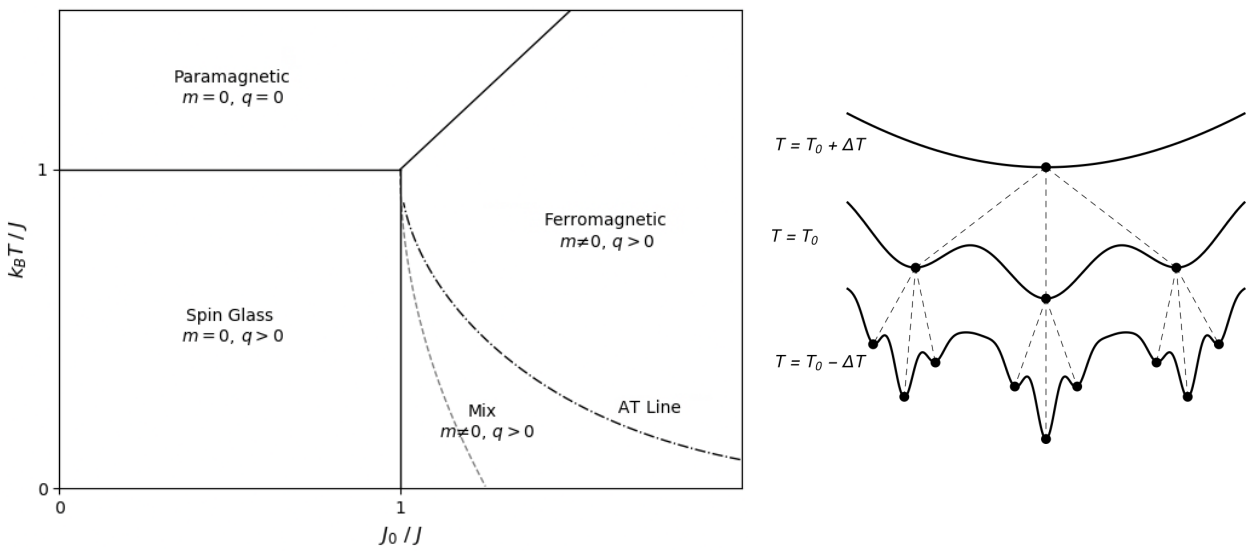

FIG. 5: Left: Phase diagram of the SK model. Below the AT line the RS solution is unstable and RSB occurs. The grey dashed line in the mixed region would separate the ferromagnetic and spin glass phases if the RS solution applied. Right: Schematic depiction of the branching process of pure spin glass states as the temperature T is lowered.

If couplings exist between all pairs of spins the model is mean-field. If, additionally, their distribution is Gaussian $J_{ij} \sim \mathcal{N}(\mu, \sigma)$ with mean $\mu = J_0/N$ and variance $\sigma^2 = J^2/N$, the resulting model is that of Sherrington-Kirkpatrick (SK) [18]. Fortunately, its free energy

$$-\beta N f\{J_{ij}\} = \ln Z\{J_{ij}\} = \ln \operatorname{Tr} e^{-\beta \mathcal{H}\{J_{ij}\}} \tag{9}$$

is *self-averaging* [19], that is,

$$\lim_{N\to\infty} f\{J_{ij}\} = \lim_{N\to\infty} [f] \qquad \text{with probability 1,} \tag{10}$$

which allows the indistinct use of f and $[f]$ in the thermodynamic limit. The latter is explicitly independent of the couplings J_{ij} and thus more convenient.

It is worth noting that the disorder average is performed *after* the ensemble average, which is known as *quenched* average. If, instead, the ensemble average takes the disorder into account (by summing over all J_{ij} configurations) then it would be *annealed*.

The precise calculation of $[f]$ in the thermodynamic limit is a highly non-trivial exercise, having only been rigorously justified twenty-five years after the model was proposed [20]. A brief heuristic outline of the main points follows [10, 21].

1. Replica trick and overlap

The first obstacle to sort is the logarithm in (9), which is done using the *replica trick*

$$\ln Z = \lim_{n\to 0} n^{-1}(Z^n - 1)\,. \tag{11}$$

While Z^n is easier to manipulate than $\ln Z$, it introduces n replicas (indexed by α),

$$[Z^n] = \left[\operatorname{Tr}\exp(-\beta\textstyle\sum_\alpha \mathcal{H}_\alpha)\right], \qquad \mathcal{H}_\alpha = \mathcal{H}\{s_i^\alpha\}\,, \qquad \alpha = 1,..,n \tag{12}$$

which may seem like a mere calculation artifact. The replicas, however, do have a clear physical interpretation: they are independent instances of the system under a given (quenched) disorder that act as samples of the energy landscape, thus encoding its structure in the correlations $q_{\alpha\beta} = [\langle s^\alpha s^\beta\rangle]$ between them, commonly referred to as *overlaps*.

Moreover, these overlaps constitute a second order parameter (the first being the magnetisations m_α). The need for a second order parameter can intuitively be understood by inspection of the phase diagram (figure 5). As in the Lenz–Ising model, the magnetisation m clearly distinguishes the paramagnetic ($m = 0$) and ferromagnetic ($m \neq 0$) phases when the disorder is mild ($J < J_0$). On the other hand, when the disorder is relevant ($J > J_0$) both the high and low temperature phases satisfy $m = 0$, yet for completely different reasons.

The difference is, naturally, in their dynamics. In the paramagnetic phase, the kinetic energy is dominant, spins are "boiling" randomly, and there are no correlations between spins within a replica ($m = 0$) or across replicas ($q = 0$). On the other hand, in the spin glass phase, the kinetic energy cannot overcome the couplings and spins are "frozen" into seemingly random configurations, with no correlations between spins within a replica ($m = 0$). However, the configurations are not really random, but instead follow from the underlying frustrated interactions, which remain the same across replicas, thus producing correlations across them ($q > 0$).

Mathematically, the order parameters are extracted from (12) in two steps. Firstly, the problem is reduced to a single-body one by linearising the quadratic terms of $\mathcal{H}_\alpha$ with the Gaussian integral formula, thus replacing interactions between spins with interactions with common fluctuating scalar fields $q_{\alpha\beta}$ and m_α. Secondly, the saddle-point method is used in the thermodynamic limit, transforming the fields into order parameters. The result is

$$\beta f = \lim_{n\to 0}\left\{ \frac{\beta^2 J^2}{2n}\sum_{\alpha<\beta} q_{\alpha\beta}^2 + \frac{\beta J_0}{2n}\sum_\alpha m_\alpha^2 - \frac{\beta^2 J^2}{4} - \frac{1}{n}\ln\operatorname{Tr} e^L \right\}, \tag{13}$$

where, for any spin s (since they are all equivalent by symmetry),

$$L = \beta^2 J^2 \sum_{\alpha<\beta} q_{\alpha\beta}\, s^\alpha s^\beta + \beta \sum_\alpha (J_0\, m_\alpha + h)\, s^\alpha \,. \tag{14}$$

Finally, by demanding stationary values of m_α and $q_{\alpha\beta}$ for $\alpha \neq \beta$,

$$\partial_{m_\alpha} f = 0 \qquad \Rightarrow \qquad m_\alpha = \frac{\operatorname{Tr} s^\alpha e^L}{\operatorname{Tr} e^L} \quad = \langle s^\alpha \rangle_L \quad = [\langle s^\alpha \rangle] \tag{15}$$

$$\partial_{q_{\alpha\beta}} f = 0 \qquad \Rightarrow \qquad q_{\alpha\beta} = \frac{\operatorname{Tr} s^\alpha s^\beta e^L}{\operatorname{Tr} e^L} = \langle s^\alpha s^\beta \rangle_L = [\langle s^\alpha s^\beta \rangle] \,, \tag{16}$$

which are now explicitly seen to be, indeed, order parameters.

2. Replica-symmetric solution

The replicas must clearly be symmetrical in the paramagnetic phase, where the energy landscape is homogeneous. Once the temperature crosses the critical temperature J/k_B metastable valleys will begin to form and ergodicity will be broken (right side of figure 5). A similar reasoning applies to the ferromagnetic phase, but accounting for its spontaneous breaking of the spin symmetry. Thus, in the bulk phases, the replica-symmetric (RS) solution must hold:

$$m_\alpha = m \,, \tag{17}$$

$$q_{\alpha\beta} = q \,, \tag{18}$$

from which (13) becomes

$$-\beta f = \frac{\beta^2 J^2}{4} (1-q)^2 - \frac{\beta J_0}{2} m^2 + \int Dz\, \ln 2 \cosh \beta \tilde{H}(z) \,, \tag{19}$$

where $Dz = (2\pi e^{z^2})^{-1/2}\, \mathrm{d}z$ is the Gaussian measure and $\tilde{H}(z) = J\sqrt{q}\, z + J_0\, m + h$. Also, the order parameters (15) become

$$m = \int Dz\, \tanh \beta \tilde{H}(z) \,, \tag{20}$$

$$q = \int Dz \left(\tanh \beta \tilde{H}(z)\right)^2 . \tag{21}$$

which are worth reading together with figure 5.

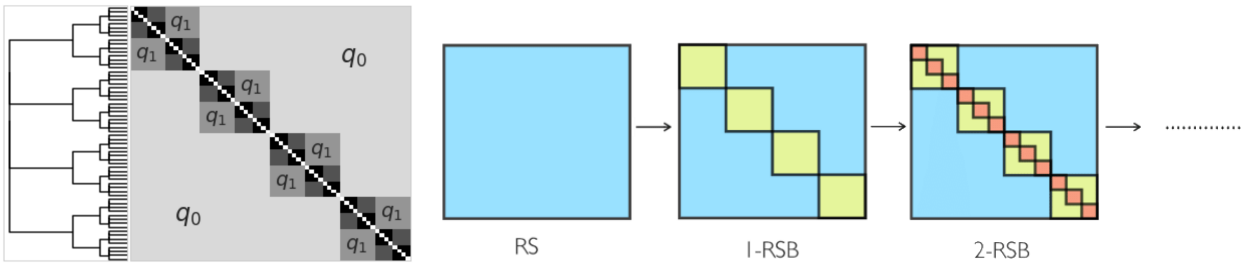

FIG. 6: Left: The block-diagonal RSB solution for the overlap matrices q_{ab} with a dendrogram on its left side illustrating its hierarchical structure. From [22]. Right: A schematic representation of the RSB scheme. From [23].

3. Replica symmetry breaking

The RS solution is, naturally, not expected to be valid everywhere—in particular it should not be applicable in the pure spin glass phase. Indeed, by performing stability analysis, the RS solution is found to be valid when the following inequality is satisfied:

$$1 > \beta^2 J^2 \int Dz \, \mathrm{sech}^4(\beta J \sqrt{q} z + \beta J_0 m) \, . \tag{22}$$

This condition defines the Almeida-Thouless (AT) line [24], under which the RS solution is unstable (figure 5). It signals the off-set of the myriad-valley structure, non-ergodicity, irreversibility and, importantly, replica-symmetry breaking (RSB).

Parisi's RSB solution [25] sequentially breaks down the overlaps between replicas $q_{\alpha\beta}$ into nested, hierarchical domains (figure 6) as follows: First, the homogeneous matrix $q^{\alpha\beta} = q_0$ for $\alpha \neq \beta$, of dimension $n \times n$, is subdivided into blocks of side length m_1. Then, the block-diagonal elements are set to the value q_1. The procedure then iterates: subdivision into blocks of side length m_1/m_2, block-diagonal elements are set to q_2 and repeat. A sequence

$$n = m_0 > m_1 > m_2 > ... > m_{K+1} = 1 \tag{23}$$

is thus generated, along with the piece-wise step function

$$q(x) = q_i \, , \qquad 1 < m_{i+1} < x < m_i < n \, , \qquad m_i \in \mathbb{Z}_{\geq 0} \, . \tag{24}$$

The shocking twist is that the sequence order will be inverted as $n \to 0$ and the piece-wise step function will become continuous over the unit interval. This is the essence of Parisi's RSB solution.

A brief outline of how the free energy f_{RSB} is obtained follows. As an example, consider the term $q_{\alpha\beta}^2$ in (13). At order K of the RSB process, it reads (figure 6)

$$\sum_{\alpha\neq\beta} q_{\alpha\beta}^l = n \sum_{0\leq i\leq K} (n_i - n_{i+1})\, q_i^l\,, \qquad \text{for} \quad l \in \mathbb{Z}_{\geq 0}\,. \tag{25}$$

Then, replacing $n_i - n_{i+1} \to -\,\mathrm{d}x$ and taking the limits $K \to \infty$ and $n \to 0$,

$$\lim_{n\to 0} \frac{1}{n} \sum_{a\neq b} q_{\alpha\beta}^l = -\int_0^1 \mathrm{d}x\; q^l(x)\,, \tag{26}$$

from where the distribution of the overlaps $P(q) = [P_J(q)]$ can be read

$$\bar{q} = \int_0^1 q(x)\,\mathrm{d}x = \int_0^1 q' P(q')\,\mathrm{d}q' \quad \Rightarrow \quad P(q) = \frac{\mathrm{d}x}{\mathrm{d}q}\,, \quad x(q) = \int_0^q P(q')\,\mathrm{d}q'\,. \tag{27}$$

In the special case $J_0 = 0$ (thus $m = 0$), equivalent (albeit harder) RSB calculations for (14) eventually lead to the following system of equations [21, p. 217]

$$-\beta f_{\mathrm{RSB}} = \tfrac{1}{4}\beta^2 J^2 \Big\{ 1 - 2q(1) + \int_0^1 \mathrm{d}x\; q(x)^2 \Big\} + \int \mathrm{D}u\; f_0\big(0, u\sqrt{q(0)}\,\big)\,, \tag{28}$$

$$\partial_x f_0(x,h)\,\mathrm{d}x = -\tfrac{1}{2} J^2 \big\{ \partial_h^2 f_0 + x\,(\partial_h f_0)^2 \big\}\,\mathrm{d}q\,, \tag{29}$$

$$f_0(1,h) = \ln 2\cosh \beta h\,. \tag{30}$$

4. Ultrametricity

Ultrametricity naturally arises in strictly hierarchical spaces. In precise terms, a metric space M is said to be ultrametric if its metric $d\colon M \times M \to \mathbb{R}_{\geq 0}$ satisfies the ultrametric or strong triangle inequality

$$d(x,z) \leq \max\{\, d(x,y), d(y,z)\,\}\,. \tag{31}$$

From this definition, the following property follows: for all $x, y, z \in M$, at least one of the three equalities $d(x,y) = d(x,z)$, $d(x,y) = d(y,z)$ or $d(x,z) = d(y,z)$ holds, that is, every triple of points in the space forms an isosceles triangle.

During this section, there have been several hints of the ultrametric structure of spin glass states. Figure 5 sketched how the multi-valley structure is formed by a hierarchical branching process of spin glass states, with ancestor states at higher temperatures related to descendant states at lower temperatures. The RSB schema itself has, by construction, an inherently ultrametric structure (figure 6). These intuitions are now formalised.

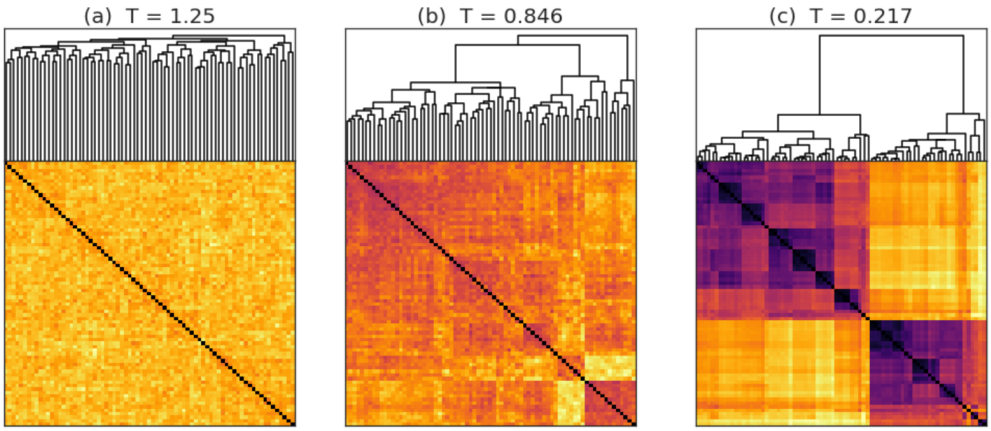

FIG. 7: Visual depictions of the ultrametric structure, or lack thereof, in the state space of the bipartite SK model for different temperatures and $J = 1$, $J_0 = 0$. The first temperature (a) corresponds to the paramagnetic (disordered) phase, and the (b,c) others correspond to the spin glass (ordered) phase. The darker the colour the higher the overlap. From [22].

Equation (27) may be derived by defining

$$P_J(q) = \langle \delta(q_{\alpha\beta} - q) \rangle = \sum_{\alpha,\beta} P_\alpha P_\beta \, \delta(q_{\alpha\beta} - q) \,, \tag{32}$$

and applying to it the RSB method. Similarly, one may define,

$$P_J(q_1, q_2, q_3) = \sum_{\alpha,\beta,\gamma} P_\alpha P_\beta P_\gamma \, \delta(q_{\alpha\beta} - q_1) \, \delta(q_{\beta\gamma} - q_2) \, \delta(q_{\gamma\alpha} - q_3) \,, \tag{33}$$

and apply the RSB method to obtain

$$\begin{aligned} P(q_1, q_2, q_3) = [P_J(q_1, q_2, q_3)] = \tfrac{1}{2} \, x(q_1) \, P(q_1) \, \delta(q_1 - q_2) \, \delta(q_2 - q_3) \\ + \tfrac{1}{2} \, P(q_1) \, P(q_2) \, \theta(q_1 - q_2) \, \delta(q_2 - q_3) \\ + \tfrac{1}{2} \, P(q_2) \, P(q_3) \, \theta(q_2 - q_3) \, \delta(q_3 - q_1) \\ + \tfrac{1}{2} \, P(q_3) \, P(q_1) \, \theta(q_3 - q_1) \, \delta(q_1 - q_2) \,, \end{aligned} \tag{34}$$

where θ is the Heaviside step function. $P(q_1, q_2, q_3)$ is ultrametric as it satisfies equation (31).

The ultrametricity of the SK model has only been rigorously proved recently [26]. Before then—and also after—direct simulations to assess ultrametricity have been performed. Many of them [22, 27–29] have depicted individual samples of the overlap matrices, and dendrograms to represent the hierarchical clustering (figure 7). Details on these methods are provided in §III.

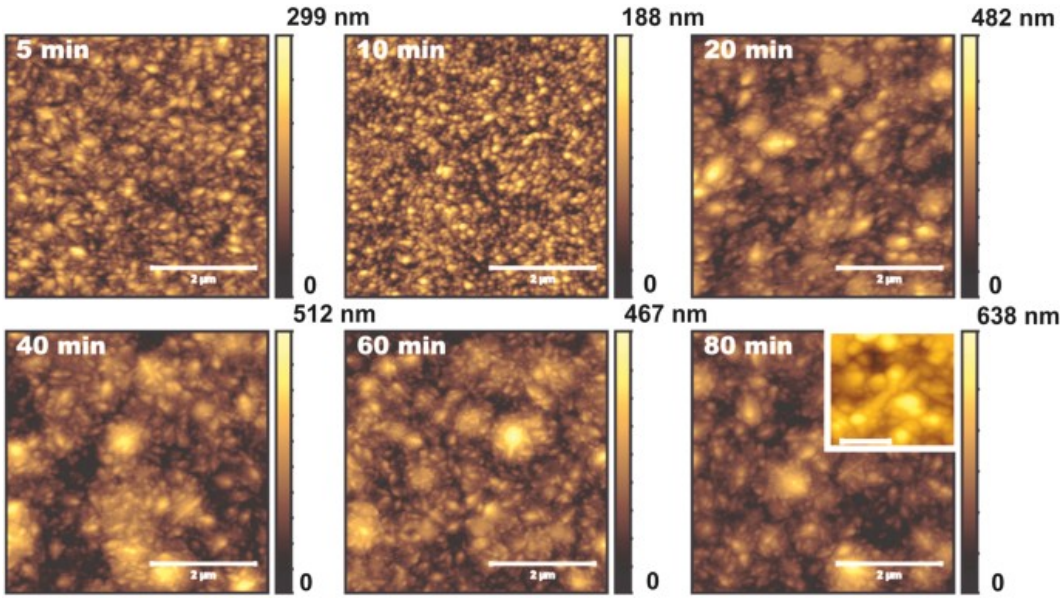

FIG. 8: Images of electrodeposited alloy films for different times. At sufficiently long times, the fluctuations of their surfaces are in the KPZ universality class. From [31].

C. Non-equilibrium systems: surface growth in first-passage percolation

Scale invariance is not restricted to thermal equilibrium systems (§II A), or out-of-equilibrium systems (§II B), but can also be found in non-equilibrium systems.

These are different from out-of-equilibrium systems in that the latter are described by a Hamiltonian and their stationary states are extrema of its Gibbs measure. They are not in equilibrium because either they were driven away from it, or are simply unable to reach it (as is the case with spin glasses and their ultrametric ergodicity breaking §II B).

Non-equilibrium systems, however, do not have hermitian Hamiltonians. If defined by transition rates, these will not satisfy detailed balance. If they have steady states, these are not given by a Gibbs measure [30]. They can even be genuinely non-equilibrium models, in the sense that they are unrelated to equilibrium. Our classes of interest, those of interface growth, are of this kind.

Growth phenomena have allowed the scientific community to address the fundamental issues of scale invariance and universality by allowing the resolution of very fine fluctuations, both experimentally and theoretically [5, 31, 35–37] (figures 2, 3, 8, 9 and 10).

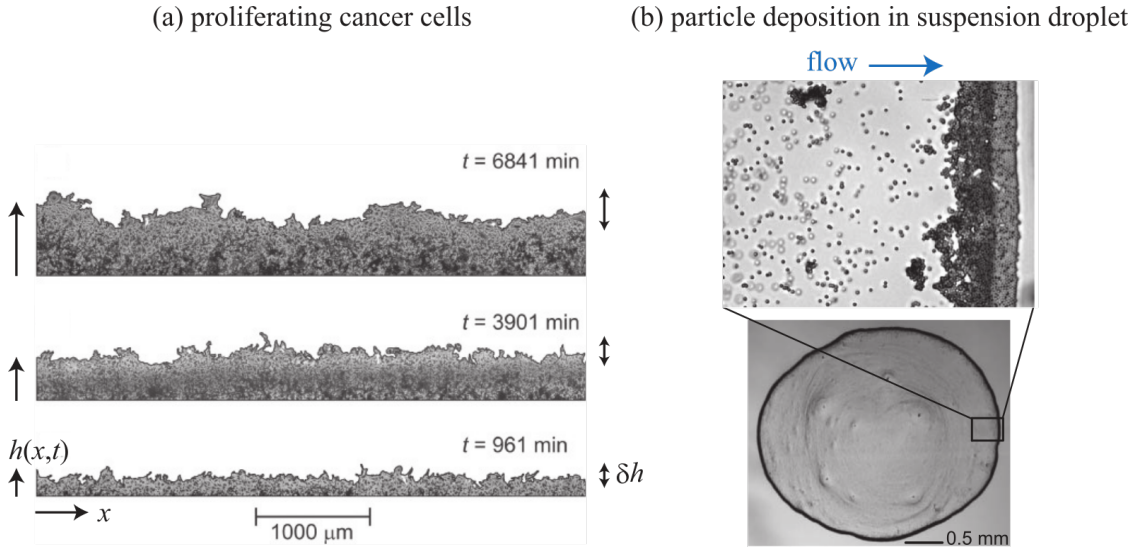

FIG. 9: Experimental examples of growing interfaces found to scale as 1D KPZ. (a) Front evolution of cancer cell colonies cultured in Petri dishes [32]. (b) Deposition of spherical colloid particles onto the edge of a suspension droplet, during its evaporation process [33]. 1D KPZ exponents were observed when using slightly elongated particles. From [34].

1. *Kardar–Parisi–Zhang universality class*

The scale invariance in all these phenomena lies in the fractal-like roughness of their growing interfaces, which is now characterised.

Let $h(x,t)$ be the local *height* of the interface along its growth direction (figures 9 and 10). Then, its standard deviation over a length scale L is a measure of the interface roughness, commonly referred to as its *width*, that is,

$$w(L,t) = \left\langle \left\langle h^2 - \langle h \rangle_L^2 \right\rangle_L^{1/2} \right\rangle , \tag{35}$$

where $\langle \cdots \rangle_L$ denotes the average over a length L and $\langle \cdots \rangle$ the unrestricted average along the complete interface. This width is often observed to satisfy the Family-Vicsek scaling:

$$w(L,t) \sim t^{\beta} F\big(Lt^{-1/z}\big) \sim \begin{cases} L^{\alpha} & \text{for } L \ll L^* , \\ L^{\beta} & \text{for } L \gg L^* . \end{cases} \tag{36}$$

where F is a universal function, $L^* \sim t^{1/z}$ a crossover length, β is the *growth* exponent and $z = \alpha/\beta$ the *dynamic* exponent. For instance, the one-dimensional exponents are $\beta = 1/3$ and $z = 3/2$. Indeed, this scaling law is satisfied by many of the aforementioned figures in this section, such as 9 and 10.

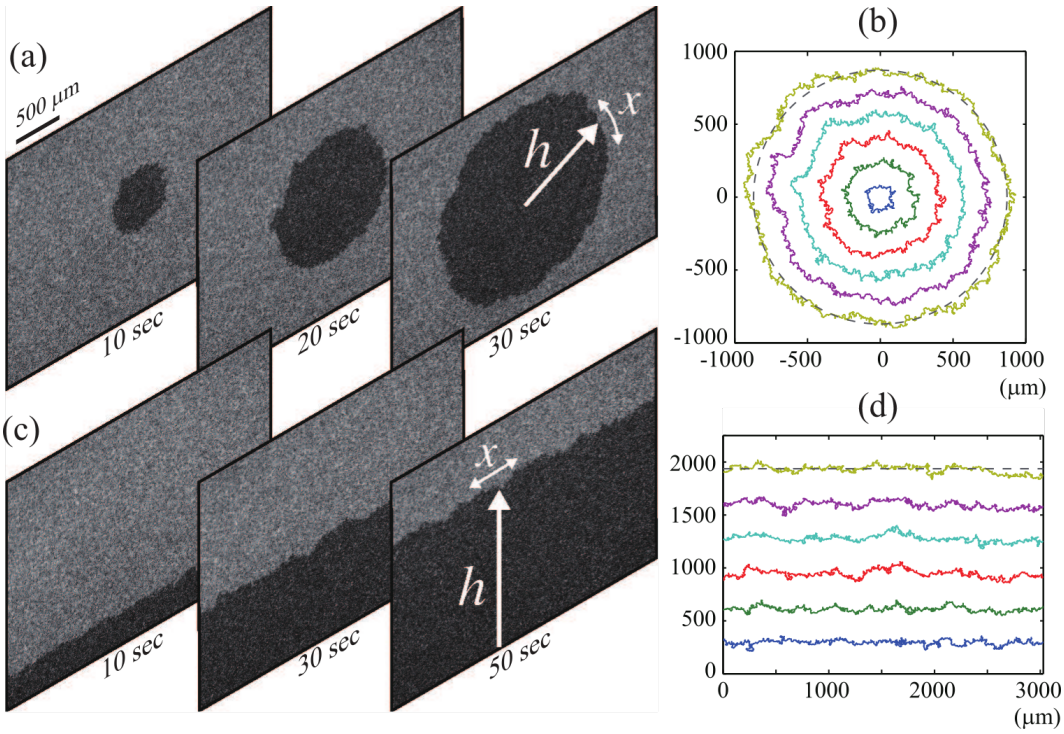

FIG. 10: Growing cluster in liquid-crystal turbulence, with both a circular (a,b) and flat (c,d) interface. (a, c) Raw images at different times. (b, d) Snapshots of the interfaces at different times. Their fluctuations follow KPZ scaling and asymptotically agree precisely with solvable models of the KPZ class. From [35]

This universality class is well understood on account of its most well-known member, the Kardar–Parisi–Zhang (KPZ) equation [38], and is thus referred to as the KPZ universality class. The equation reads

$$\partial_t h = \nu \nabla^2 h + \tfrac{1}{2}\lambda(\nabla h)^2 + \sqrt{D}\,\eta(x,t)\,,$$

where α, ν, D scalar parameters and η is white Gaussian noise that can be thought of as representing random nucleation events in the interfacial growth.

2. *First-passage percolation model*

As mentioned in §I, one of the best-known growth models is the first-passage percolation (FPP) model [39], which describes the single-source spread of geodesics in random graphs, and whose scaling behaviour is described the KPZ universality class (figures 2, 3 and 11).

The model is defined as follows. Let $\mathcal{G} = (\mathcal{V}, \mathcal{E}, t)$ be a weighted graph of nodes $\mathcal{V}$, links

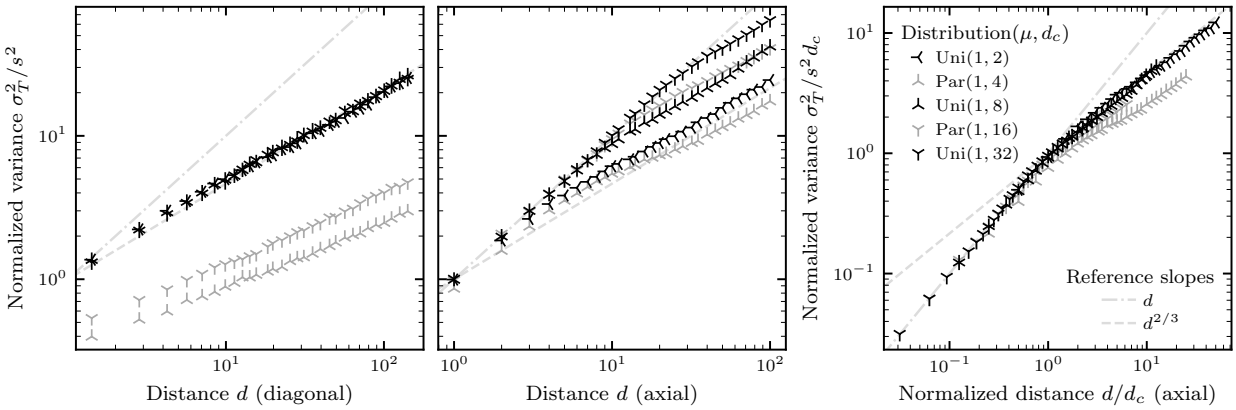

FIG. 11: Scaling of the variance of the minimal arrival time σ_T with the Euclidean distance d. Results are from 4000 random realizations of the weights t.

$\mathcal{E} \subseteq \mathcal{V}^2$ and quenched random link-times $t\colon \mathcal{E} \to \mathbb{R}_{\geq 0}$. Then, a path γ of length $n = |\gamma|$ is a sequence of nodes $(v_0, .., v_n) \in \mathcal{V}^{n+1}$ such that all links $e_i = (v_{i-1}, v_i) \in \mathcal{E}$ and are unique. If also the nodes are unique, then the path is simple (loopless). Moreover, a *time* geodesic from node v to w is a path $\gamma^*_{vw} = (v, .., w)$ that minimizes the arrival time $t(\gamma) = \sum_{e_i \in \gamma} t(e_i)$, while a *space* (or Euclidean) geodesic minimizes n. The set of nodes that can be reached under a time τ starting from a node $v \in \mathcal{V}$ is the ball $B_v(\tau) = \{w \in \mathcal{V} : T_v(w) < \tau\}$ where $T_v(w) = t(\gamma^*_{vw})$ is the minimal arrival time. These induce a metric on $\mathcal{G}$ that is random by virtue of the quenched realizations of the link-times t.

The lateral spread (or deviation) $\delta_\perp$ of a time geodesic can then be characterized as the minimum distance from its timewise midpoint to the corresponding space geodesic. Further, the width of a ball $B_v(\tau)$ at time τ can be characterized as the standard deviation of its interface around its mean position at time τ.

This work is concerned a different (possibly related) quantity: the standard deviation of the minimal arrival time σ_T. There is supporting evidence [37] that, in isotropic continuous random media, the width of a ball of radius d centred at v is equivalent to the σ_T of any point at Euclidean distance d from v. For discrete media, it is still an open problem.

Indeed, the asymptotic behavior of the FPP model for both $\delta_\perp$ and σ_T as $d \to \infty$ follows the KPZ universality class regardless of the link-time probability distribution and of the lattice topology. Pre-asymptotic behavior, on the other hand, depends on the degeneracy of space geodesics [5].

In particular, for square lattices, the degree of geodesic degeneracy between points on a

diagonal is maximal and equal to $n!/(n/2)!^2$, and the pre-asymptotic regime is negligible. On the other hand, on an axis it is minimal and equal to one, and the pre-asymptotic regime lasts until a critical distance

$$d_c = \frac{1}{3}\frac{\mu^2}{s^2}\,,$$

where μ is the mean of the probability distribution of the link-times and s^2 is its variance. It is worth noting that the coefficient of variation (here s/μ) also plays an important role in the SK model (there J/J_0), where it distinguishes mixed and spin glass phases at low temperatures (figure 5).

These results have been reproduced for σ_T and are reported in figure 11. They have been generated using the Dijkstra algorithm [40] (algorithm 1) to calculate the geodesics and a permuted congruential generator [41] to pseudo-randomly generate the link-times, which were distributed which followed one of two distributions:

- Uniform distribution, denoted $\mathrm{Uni}(t_0, t_1)$ for $t_0, t_1 \in \mathbb{R}$, and whose PDF is constant in $[t_0, t_1]$. Its moments are $\mu_n = (b^{n+1} - a^{n+1})\,(b-a)^{-1}(n+1)^{-1}$.

- Pareto distribution, denoted $\mathrm{Par}(t_0, \alpha)$ for $t_0, \alpha \in \mathbb{R}^+$, and whose PDF is $\alpha t_0^\alpha / t^{\alpha+1}$ for $t \in [t_0, \infty)$. Its moments are $\mu_n = \alpha t_0^n (\alpha - n)^{-1}$ for $\alpha > n$ and ∞ otherwise.

They were chosen because their support is positive and belong to different Mandelbrot states of randomness [42] (the uniform distribution is mild while the Pareto one is pre-wild).

D. The *k* shortest simple paths problem

1. *Shortest path*

Being a fundamental optimization problem of extensive practical application, the shortest path problem between two given vertices has been amply studied and is well understood. As this work is solely concerned with positively-weighted undirected graphs, this section is restricted to them too.

In this domain, the unavoidable reference is Dijkstra's shortest path algorithm [40], whose time complexity is $\mathcal{O}(V^2)$. Beginning from the source node v_a, the algorithm percolates the graph until the target node v_b is reached (algorithm 1). For sparse connected graphs—such

as square lattices—storing the graph as an adjacency list and the active nodes as a priority queue improves the complexity to $\mathcal{O}(E \log V)$.

Moreover, performance improvements can be implemented that, while not decreasing the complexity, tend to be faster in practice. For instance, the A* algorithm [43] improves

---

ALG. 1: A* variant of Dijkstra's shortest path algorithm.

Inputs:

- Weighted graph $\mathcal{G} = (\mathcal{V}, \mathcal{E}, t)$ of nodes $\mathcal{V}$, links $\mathcal{E} \subseteq \mathcal{V}^2$ and link-times $t\colon \mathcal{E} \to \mathbb{R}_{\geq 0}$.
- Source and target nodes $v_a, v_b \in \mathcal{V}$.
- An admissible heuristic $h_b\colon \mathcal{V} \to \mathbb{R}_{\geq 0}$. Dijkstra's original algorithm corresponds to $h_b = 0$.

function AStarSP($\mathcal{G}, v_a, v_b, h_b$)
  for each node $v \in \mathcal{V}$ **do**
    $T_a(v) \leftarrow \infty$ ▷ *Minimum time from v_a*
    $p_a(v) \leftarrow \varnothing$ ▷ *Parent in shortest path from v_a*
  $T_a(v_a) \leftarrow 0$
  $\mathcal{A} \leftarrow \{v_a\}$ ▷ *Active nodes*
  $v \leftarrow v_a$ ▷ *Current node*
  while $v \neq v_b$ **and** $\mathcal{A} \neq \varnothing$ **do**
    $\mathcal{A} \leftarrow \mathcal{A} \setminus \{v\}$
    for each node w such that $(v, w) \in \mathcal{E}$ **do**
      $t' \leftarrow T_a(v) + t(v, w)$
      if $t' < T_a(w)$ **then**
        $T_a(w) \leftarrow t'$
        $p_a(w) \leftarrow v$
        $\mathcal{A} \leftarrow \mathcal{A} \cup \{w\}$
    $v \leftarrow v \in \mathcal{A}$ that minimises $T_a(v) + h_b(v)$
  $n \leftarrow n \in \mathbb{N}$ such that $v_a = p_a^n(v_b) = p_a(p_a^{n-1}(v_b))$
  return $\big(p_a^j(v_b) : j \in (n, \ldots, 0)\big)$

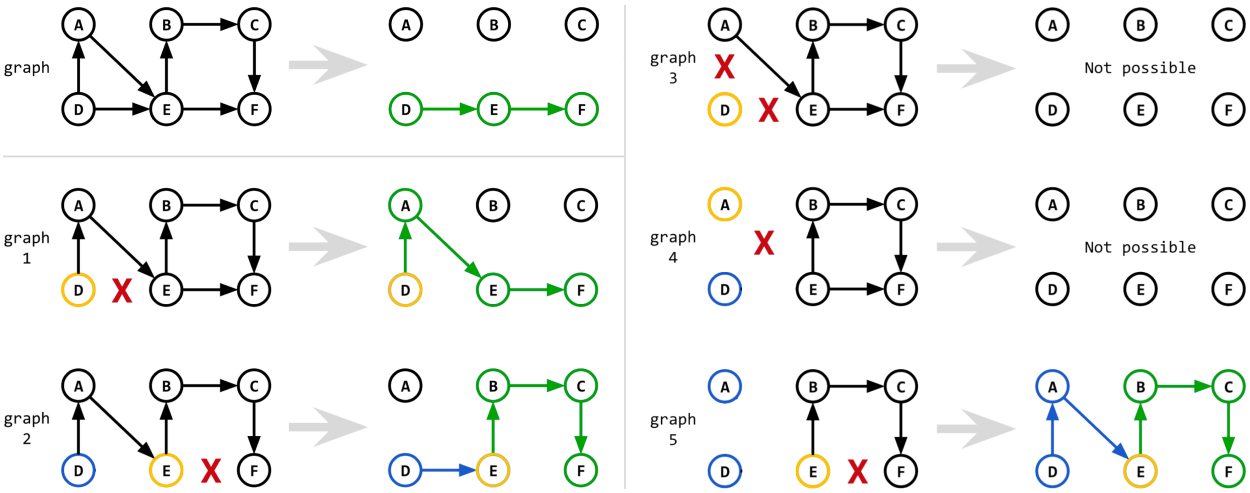

FIG. 12: An example of Yen's kSSP algorithm up to $k = 3$. Root paths are coloured in blue, spur paths in green, and spur nodes in yellow. Adapted from [47].

the prioritisation of active nodes by incorporating a heuristic function $h_b \colon \mathcal{V} \to \mathbb{R}_{\geq 0}$ that estimates the minimum time from any node v to the target node v_b (algorithm 1). To guarantee correctness, the heuristic must be *admissible*, that is, an upper bound of the actual minimum time to v_b.

2. *Ranking shortest paths*

The ranking of shortest paths is a natural generalisation of the shortest path problem. Indeed, the first article on the topic [44] was published in 1959, around the time of Dijkstra's own article on his shortest path algorithm [40]. While the generalisation has been less studied than the base problem, it still has drawn enough interest to produce algorithms with very different approaches along with several optimizations.

Since only positive weights are being considered, the shortest path is necessarily simple (loopless). This is, however, not the case for the k shortest paths. If unrestricted (loopy) paths are allowed, the foundational algorithm is then Eppstein's sidetrack-based algorithm [45], whose time complexity is $\mathcal{O}(E + V \log V + k)$.

Loopless paths, however, have been deemed more physically meaningful within the scope of this work, so this section will focus on them. In this case, the main algorithm is due to Yen [46], whose time complexity depends on the shortest path subroutine used, but is usually taken to be $\mathcal{O}(kV(E + V \log V))$.

Yen's algorithm generates the k shortest simple path (SSP) by sequentially removing each edge from the $(k-1)$SSP and solving the shortest path problem in the modified graph (accounting for previous paths which might have generated it first). Then, from all the candidates generated in this and previous iterations, the shortest one will be the kSSP. A simple example is provided in figure 12 and explained here:

1. Graph 0. The shortest path P_1 of the original graph is DEF.

2. Graphs 1–2. To obtain P_2^1 (the first candidate for P_2) the first edge DE of P_1 is removed from the graph. The shortest path of the modified graph is then $P_2^1 = \text{DAEF}$. Similarly, $P_2^2 = \text{DEBCF}$ is obtained by also removing the second edge EF of P_1 and solving from the next node E to the target F. In the example, the shortest of the two candidates turns out to be $P_2 = P_2^1$.

3. Graphs 3–5. To obtain $P_3^1 = \varnothing$ the first edge DA of P_2 must be removed, but also DE because it was used by P_1. Removing also the second edge AE allows no path from the next node A to the target F, so $P_3^2 = \varnothing$. Finally, removing the third edge EF does produce a path $P_3^3 = DAEBCF$. The third shortest path P_3 is then the shortest of the two candidates P_2^2 and P_3^3.

When solving each shortest path sub-problem, the source node is referred to as the *spur node*, and the minimal path to the target the *spur path*. The resulting candidate path is obtained by concatenating the spur path with the *root path*, which comprises the spur nodes that have previously been processed (figure 12).

A straightforward time optimization due to Lawler [48] avoids generating trivially duplicate candidates: when obtaining P_k, it is not necessary to remove every edge of P_{k-1}, but only those in its spur path, that is, the path between its spur node and the target. Moreover, further duplicates can only occur in the spur node itself, which greatly narrows the required checks (algorithm 2).

Space complexity can also be quite heavy, specially in a naive implementation. First and foremost, it is not necessary to store all paths: only k are needed at any given time. Secondly, it is possible (even natural) to synergise the calculation procedure with the main data structure by storing the candidate paths in a radix trie (also known as compact prefix tree), a type of space-optimized search tree in which the children of a node share the same

ALG. 2: Yen's k shortest simple paths algorithm with Lawler's optimization.

Inputs:

- Weighted graph $\mathcal{G} = (\mathcal{V}, \mathcal{E}, t)$ of nodes $\mathcal{V}$, links $\mathcal{E} \subseteq \mathcal{V}^2$ and link-times $t \colon \mathcal{E} \to \mathbb{R}_{\geq 0}$.
- Source and target nodes $v_a, v_b \in \mathcal{V}$.
- Number of shortest paths $K \in \mathbb{Z}_{>0}$.
- A shortest path algorithm, e.g., algorithm 1.

1: **function** YenKSSP($\mathcal{G}$, v_a, v_b, K)
2: $P_1 \leftarrow S_1 \leftarrow$ ShortestPath($\mathcal{G}$, v_a, v_b)
3: $\mathcal{C} \leftarrow \varnothing$ ▷ *Candidate paths*
4: **for** each $k \in (2, .., K)$ **do**
5: $k' \leftarrow (k-1)$; $R \leftarrow \varnothing$; $\mathcal{V}' \leftarrow \mathcal{V}$; $\mathcal{E}' \leftarrow \mathcal{E}$
6: **for** each link $e \leftarrow (v, w) \in S_{k-1}$ **do**
7: $\mathcal{E}' \leftarrow \mathcal{E}' \setminus e$ ▷ *Remove current edge*
8: **while** v is the first node of $S_{k'}$ **do** ▷ *Remove edges used by ancestors*
9: $k' \leftarrow i$ such that $P^{\circ}_{i+1} = P_{k'}$ for some $\circ \in \mathcal{E}$ ▷ *Index of the parent of $P_{k'}$*
10: $e' \leftarrow$ the edge $(v, \circ) \in S_{k'}$ for some $\circ \in \mathcal{V}$
11: $\mathcal{E}' \leftarrow \mathcal{E}' \setminus e'$
12: $\mathcal{G}' \leftarrow (\mathcal{V}', \mathcal{E}', t)$
13: $S^e_k \leftarrow$ ShortestPath($\mathcal{G}'$, v, v_b) ▷ *Spur path*
14: $P^e_k \leftarrow R \cup S^e_k$ ▷ *Concatenate root and spur*
15: $\mathcal{C} \leftarrow \mathcal{C} \cup \{P^e_k\}$
16: $R \leftarrow R \cup (e)$
17: $\mathcal{V}' \leftarrow \mathcal{V}' \setminus \{v\}$
18: $P_k \leftarrow$ shortest path $P^{e^*}_{k^*} \in \mathcal{C}$
19: $S_k \leftarrow S^{e^*}_{k^*}$
20: $\mathcal{C} \leftarrow \mathcal{C} \setminus \{P_k\}$
21: **return** $(P_1, .., P_K)$

prefix up to their parent node, after which they branch. In the present case, the trie is typically an array in which each entry represents a branch of the trie, and stores the following data: 1) a reference to its parent branch, 2) its spur node—at which it branched from its parent—and 3) its spur path.

Storing the candidate paths in a trie not only reduces memory requirements, but also simplifies computations by making it very easy to retrieve spur nodes and spur paths, two of the most common operations of the algorithm [49–51].

There are many alternatives to Yen's algorithm, although only one (to our knowledge) improves its time complexity. Katoh's algorithm [52] is restricted to undirected graphs, and uses their characteristics to generate, at most, three candidates for each shortest path, resulting in a time complexity of $\mathcal{O}(k(E + V \log V))$—one order of magnitude less than Yen's. However, its constant must be significantly larger than that of Yen's, as Katoh's algorithm seems to be severely outperformed in small graphs [50].

Both Yen and Katoh's algorithms are deviation-based algorithms, but there are other approaches. For instance, Kurz's algorithm [53] is based on Eppstein's sidetrack-based approach, and seems to be faster than Yen's in practice (although with no better time complexity).

III. METHODOLOGY

The algorithms, simulations and plots described in this section and used to obtain the results in §IV can be found at https://gitlab.com/physics-complex-systems/shortest-paths.

A. Parameter variables

The different parameters used throughout the different simulations have been:

- *Grid directions*: Path endpoints located in both the diagonal (maximum geodesic degeneracy) and axial (minimum geodesic degeneracy) direction of the lattice, in the sense of [5].

- *Link-time distributions*: In order to focus the scope, only uniform distributions with mean one are used (mild randomness under Mandelbrot classification [42]). Another

reason for this choice is that wilder distributions, such as the Pareto one, have significant contributions from their tails, and thus converge much slower (figure 11).

- *Grid sizes*: Both larger and smaller than the FPP critical distance $d_c = \mu^2/3s^2$ of the link-time distributions. In every case, $d_c > 1$.

B. Shortest paths algorithm

As anticipated in the previous section (§II D), simple paths are here favoured over unrestricted ones. From the loopless algorithms, the apparently promising Katoh is discarded due to its poor performance in small graphs. Recent developments (such as Kurz's) are also discarded because optimising performance is not deemed critical at this initial stage of research.

Instead, the more intuitive algorithm of Yen is employed, enhanced with Lawler's optimization (algorithm 2). Moreover, the A* algorithm is used to accelerate the usual Dijkstra with priority queue, used by Yen's algorithm as a subroutine to calculate shortest paths. The heuristic used to bound the minimum time between nodes consists on assuming that the fastest of all edges are traversed along the path with smallest number of edges between the nodes. This simple heuristic only requires sorting the link-times and calculating their cumulative sum once per disorder realisation. Moreover, better bounds can easily be achieved by discriminating horizontal and vertical edges in the calculation.

Another time optimization has been to take advantage of the regular nature of square grids to store all link-times in a $4 \times V$ array. To prevent any irregularities in the access rules, a boundary of inaccessible nodes was added to the randomised lattice.

Regarding storage, at most k paths were being stored at any given time, and paths were stored in a radix trie, as described in §II D. Other implementation details have been drawn from various sources [49–51].

C. Overlaps and dendrograms

In order to apply the hierarchical clustering technique introduced in II B, an equivalent of the overlap $q_{\alpha\beta} \in [0, 1]$ between replicas must be defined for paths. A very natural choice is to define the overlap $q_{\alpha\beta}$ between two paths α, β as the number of edges in common divided

by the number of edges of the path with least edges, that is,

$$q_{\alpha\beta} = \frac{|\alpha \cap \beta|}{\min\{\, |\alpha|, |\beta| \,\}} \,. \tag{37}$$

Once a set of paths is obtained, dendrograms are created using hierarchical agglomerative clustering, which consists on sequentially finding the two clusters of paths which are closest, and merging them. The distance between them at the point of merging determines the height in the dendrogram. Distances between paths α, β are naturally defined as $d(x, y) = 1 - q_{\alpha\beta}$. Moreover, there are several ways to define the distance between two clusters A, B, of which we have favoured the so called complete-linkage (CL) metric, given by

$$d_{\mathrm{CL}}(A, B) = \max\{\, d(\alpha, \beta) : \alpha \in A \text{ and } \beta \in B \,\} \,. \tag{38}$$

The dendrogram leaves are sorted using an optimal leaf ordering algorithm that maximizes overlaps between neighbours[54]. Naturally, this leaf ordering is also used to sort the rows and columns of the overlap matrix $q_{\alpha\beta}$. Finally, a cut-off overlap $q_{\mathrm{cut}} = 0.7$ is set, at which height the dendrogram is cross-sectioned, obtaining a partition of the paths (clusters) associated to that cut-off value.

IV. RESULTS AND DISCUSSION

Firstly, in §IV A, independent samples of the proposed kth-passage percolation (KPP) model are inspected to develop a heuristic understanding of the structure of the associated k shortest simple paths (kSSP).

Secondly, in §IV B, the average overlaps of the kSSP with the shortest path are calculated to solidify this understanding.

Finally, in §IV C, the kth-arrival time fluctuations are obtained for different distances, similarly to figures 3 and 11 but with the kth SPP instead of the shortest one.

A. Samples

In order to explore individual realizations for different parameters and distances (figures 13 and 14) we use the instruments described in §III: path overlaps matrix $q_{\alpha\beta}$, dendrogram (built from complete-linkage hierarchical clustering) and the paths themselves, coloured

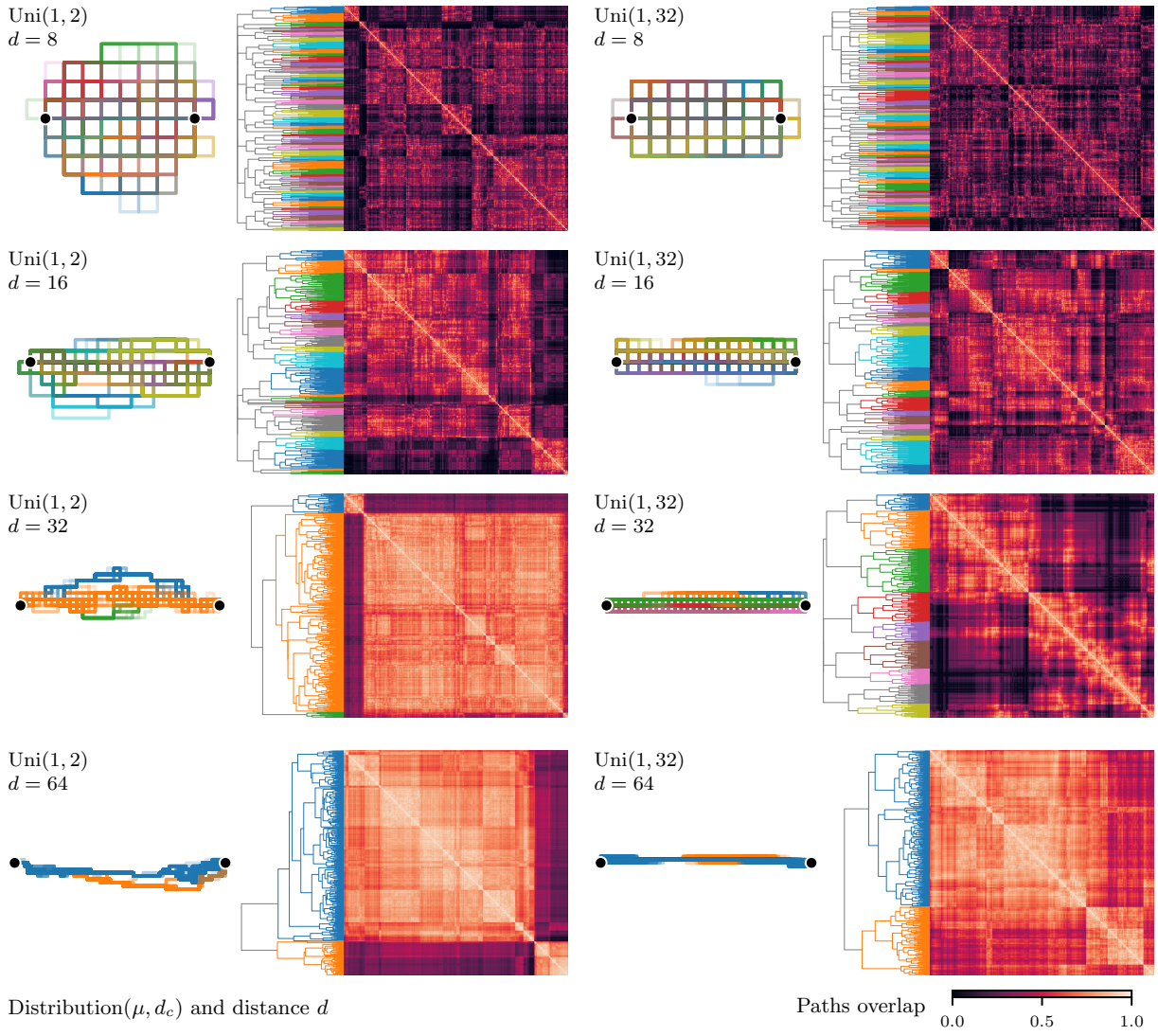

FIG. 13: Eight samples of the KPP model with different distances d between axial endpoints and link-time distributions of mean $\mu = 1$ and varying critical distances d_c. Right section of each sample: Overlaps matrix displaying path overlaps $q_{\alpha\beta}$ between the $k = 1000$ shortest paths. Paths are sorted using an optimal leaf ordering algorithm [54] that maximizes overlaps between neighbours. Mid section: Dendrogram displaying the results of complete-linkage hierarchical clustering, with a cut-off overlap $q_{\text{cut}} = 0.7$ for the colour labels. Left section: The 1000 shortest simple paths coloured according to the clusters obtained with $q_{\text{cut}} = 0.7$.

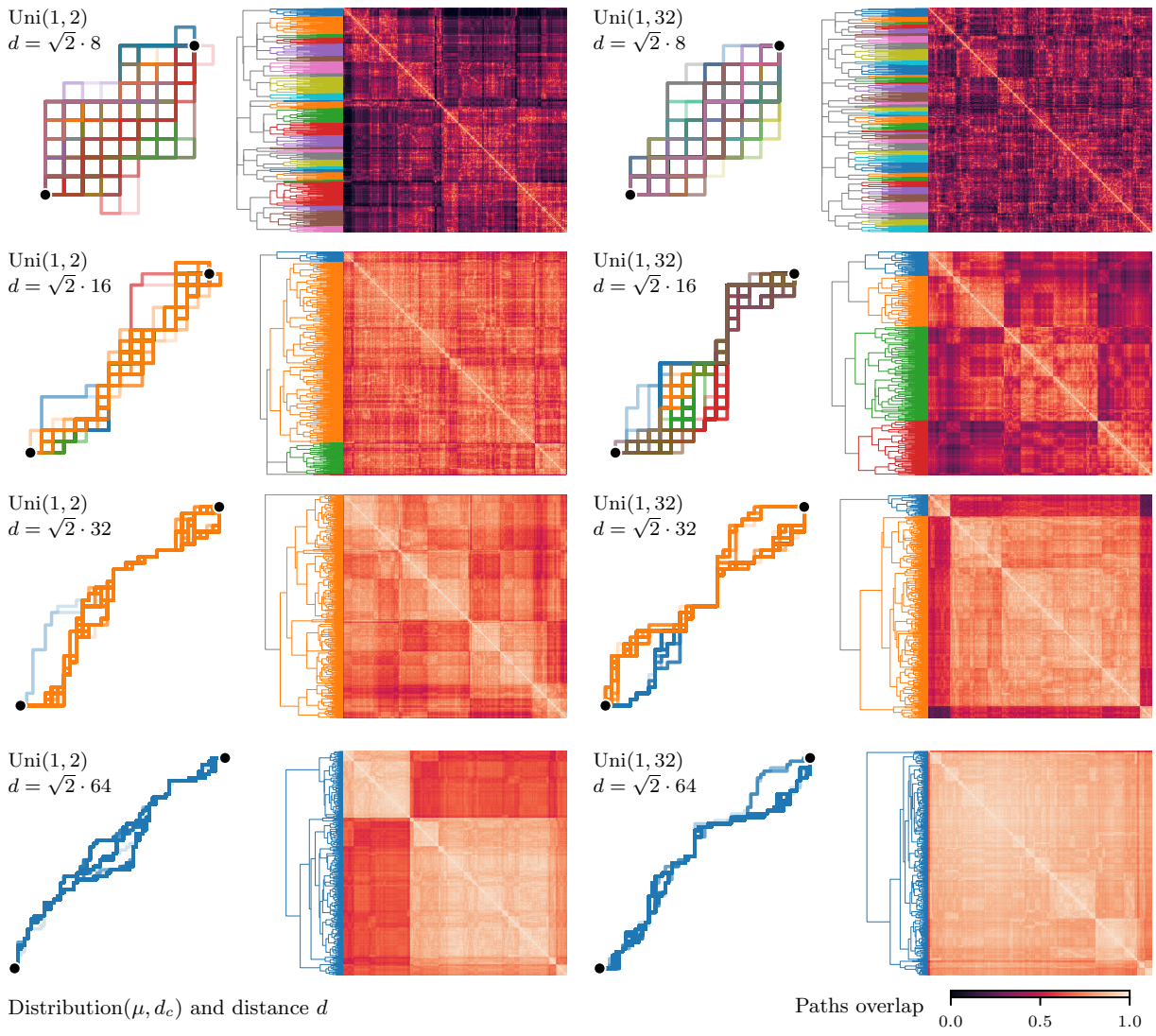

FIG. 14: Same as figure 13, but for endpoints in the diagonal.

according to the clusters associated to the dendrogram cut-off value $q_{\text{cut}} = 0.7$. The overlap between two paths is here defined as the number of common edges between two paths divided by the length of the shortest of the two paths.

The more persistent tendency is that the bigger the distance d, the higher the average overlap appears to be, as can be seen in how the clusters are formed at lower heights (this is further supported later in §IV B). Effectively, this means that the paths covered by a given number of k shortest paths become *narrower*, that is, they cover a smaller portion of the landscape, with a behaviour closer to single paths than that of a diverse set of paths. Therefore, for sufficiently big distance d the scaling should be that of KPZ, as is confirmed in §IV C.

Additionally, the cut-off $q_{\text{cut}} = 0.7$ with the complete-linkage method seems to cluster paths quite closely to what the human eye might consider appropriate (in those images were the number of clusters allows for them to be distinguished). Interestingly, the aforementioned term *narrow* is relevant for clusters too. Smaller distances d and standard deviations s typically result in more clusters, which is naturally interpreted as more varied minima of the landscape being explored.

Finally, during the development of this work, it was speculated that the structure revealed by the overlap matrices might be related to the theoretically ultrametric overlap matrices in spin glasses and Parisi's RSB procedure (figure 6) to explain their behaviour. It was reasoned, that the relationship with spin glasses is not unwarranted, given that paths experiment frustration too: by choosing certain links they are foregoing others.

Therefore, it was very satisfactory to eventually find published positive evidence of these conjectures, as covered in §II B. Most interestingly, the matrices in figures 13 and 14 show a chessboard-like, nested structure remarkably similar to the overlap matrices sampled in the spin glass phase (figure 7, panels b and c), and not the one sampled in the paramagnetic bulk phase (panel a), which appears homogeneous.

B. Average overlaps

After studying individual cases, we now turn our attention to averages. In particular, we first want to establish whether greater distances d imply higher average overlaps. A simple but robust way to tackle this is to consider only the overlaps with the shortest path (figure 15). Firstly, it is noticeable that the curves seem somewhat sharp, and their standard deviations are relatively narrow; hence, the 4000 iterations used seem appropriate. Secondly, the almost discrete saw pattern demands an explanation. By inspection, it is clear that lower standard deviations s (i.e., higher critical distances d_c) and smaller sizes are more likely to display a saw pattern. This trivially points to the cause: when the variance of the link-times is small, the k-shortest paths are strongly determined and, since there is a limited number of paths of a given length, plateaus are inevitably formed.

Take, for instance, the top left figure. Since $d = 2$, there will be $3 \cdot 2 = 6$ paths of length 4, and indeed the first plateau ends precisely at 6. In the top center case, $d = 8$ and so there are $9 \cdot 8 = 72$ paths of length 10, and approximately $(9 \cdot 8/2)^2 = 1296$ paths of length

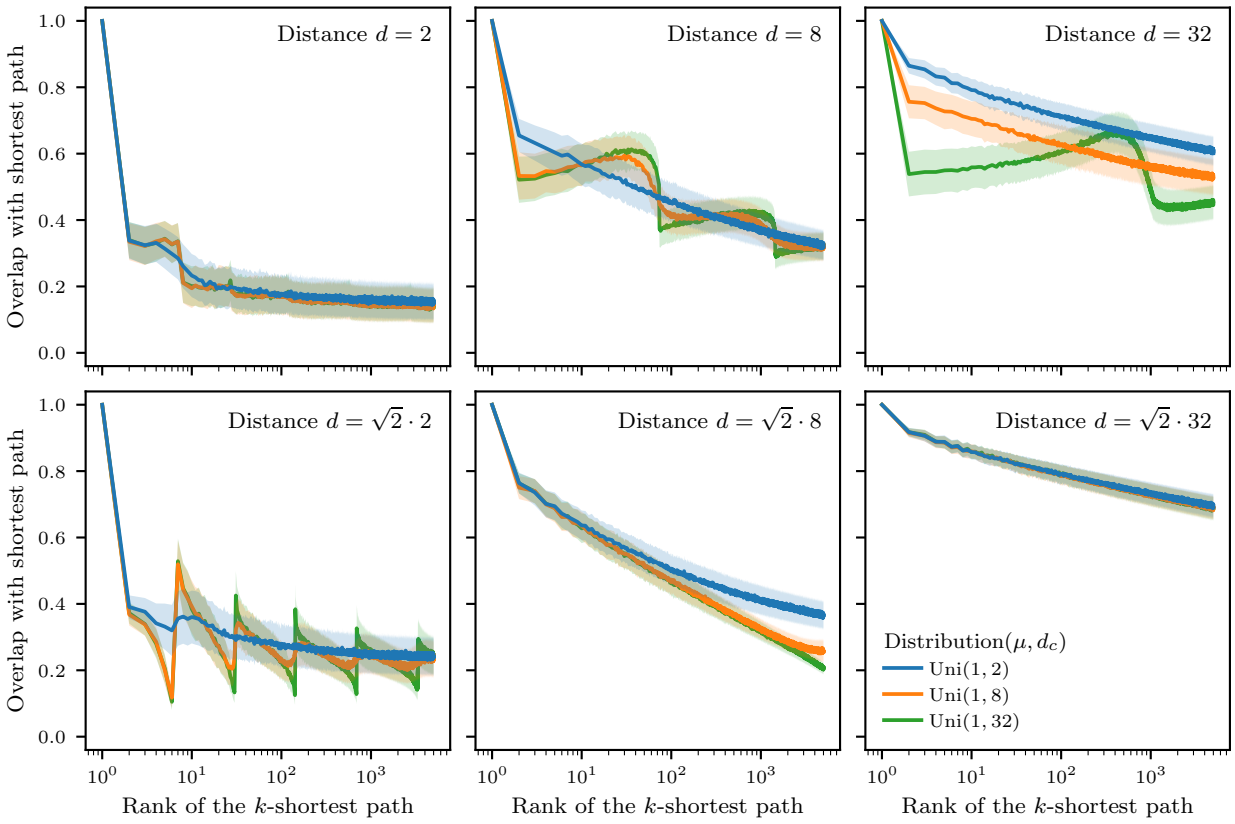

FIG. 15: Overlap with shortest path, mean (line) and standard deviation (shade). Top figures are in the axis, bottom ones in the diagonal. 4000 iterations.

12, which coincide precisely with the extent of the plateaus. It is worth noting how, in this case, the distribution with the lowest d_c (highest s) does not display the saw pattern, as it can explore the landscape more freely. For the only clear example of the diagonal case (bottom left, $d = 2\sqrt{2}$) the first plateau corresponds to the shortest paths of length 4, which coincide with the degenerate Euclidean geodesics, of which there are $(2 \cdot 2)!/2!^2 = 6$, in precise agreement with the image.

Figure 15 clearly corroborates the intuition from the previous section that the larger the distance d the larger the average overlap. Also, many of the cases very quickly fall way under the 0.7 overlap that seemed to indicate close similarity between paths, may be expected to behave differently from those that retain a high average overlap, namely those for $d = 32$, both diagonal and axial. Additionally, this might be indicative that $k = 1000$ is adequate to study small grid sizes such as those of the examples.

C. Average minimal arrival time fluctuations

Having gained confidence that 4000 iterations have sufficiently good convergence properties in studying k shortest paths for these grid sizes, and seeing how the average overlap falls very quickly too, we now reproduce the results of [5] for σ_T in square grids (figure 16).

The results follow well from previous heuristics and intuitions. First and foremost, for both the axial and diagonal directions, the pre-asymptotic regime $\sim d$ is extended with respect to that of the shortest path.

For all three distributions in the diagonal direction, results are very consistent with those of figure 15. At distance $d = \sqrt{2} \cdot 2$ (low overlap for all k) the values of $k = 10, 100, 1000$ are in the pre-asymptotic regime; at distance $d = \sqrt{2} \cdot 8$ both $k = 100, 1000$ are in the pre-asymptotic regime, but $k = 10$ has reached KPZ scaling, in agreement with the fact that the average overlap with the shortest path is close to 0.7, the cut-off overlap q_{cut} used for clustering in §II B. At $d = \sqrt{2} \cdot 32$, all ks have reached KPZ, also in agreement with all average overlaps, which at that point are all about or over 0.7. It is worth noting that different distributions have virtually no differences because, at these values of k, (almost) all k shortest paths are space geodesics, and the landscape is well explored from the very beginning regardless of the link-time variance s.

A similar analysis for the axial direction is straightforward, so we proceed in a different order. At $k = 2$ (top row of figure 16) the distribution associated to $d_c = 2$ scales as KPZ from the very moment the transient ends, the distribution of $d_c = 8$ seems to scale linearly with d until about $d \approx 30$, and the $d_c = 32$ one does not seem to abandon the pre-asymptotic until, perhaps, the very end of the reported range. These observations are consistent with the $q_{\text{cut}} = 0.7$ criteria applied to figure 15: the average overlap with the shortest path of the $d_c = 2$ distribution is about or above 0.7 for both $d = 8$ and $d = 32$, the one of $d_c = 8$ is above 0.7 for $d = 32$ and below for $d = 8$ and $d = 2$, and the $d_c = 32$ distribution is below in all three cases $d = 2, 8, 32$.

Jumping directly to $k = 1000$ (bottom row of figure 16) the pre-asymptotic regime of $d_c = 2$ ends at about $d_c \approx 30$, almost exactly when q_{cut} equals 0.7 for the $d = 32$ graph in figure 15. Similarly, the distributions $d_c = 8$ and 32, do not end their pre-asymptotic regimes until later and, consistently, their average overlap with the shortest path does not surpass 0.7 in any of the graphs of figure 15.

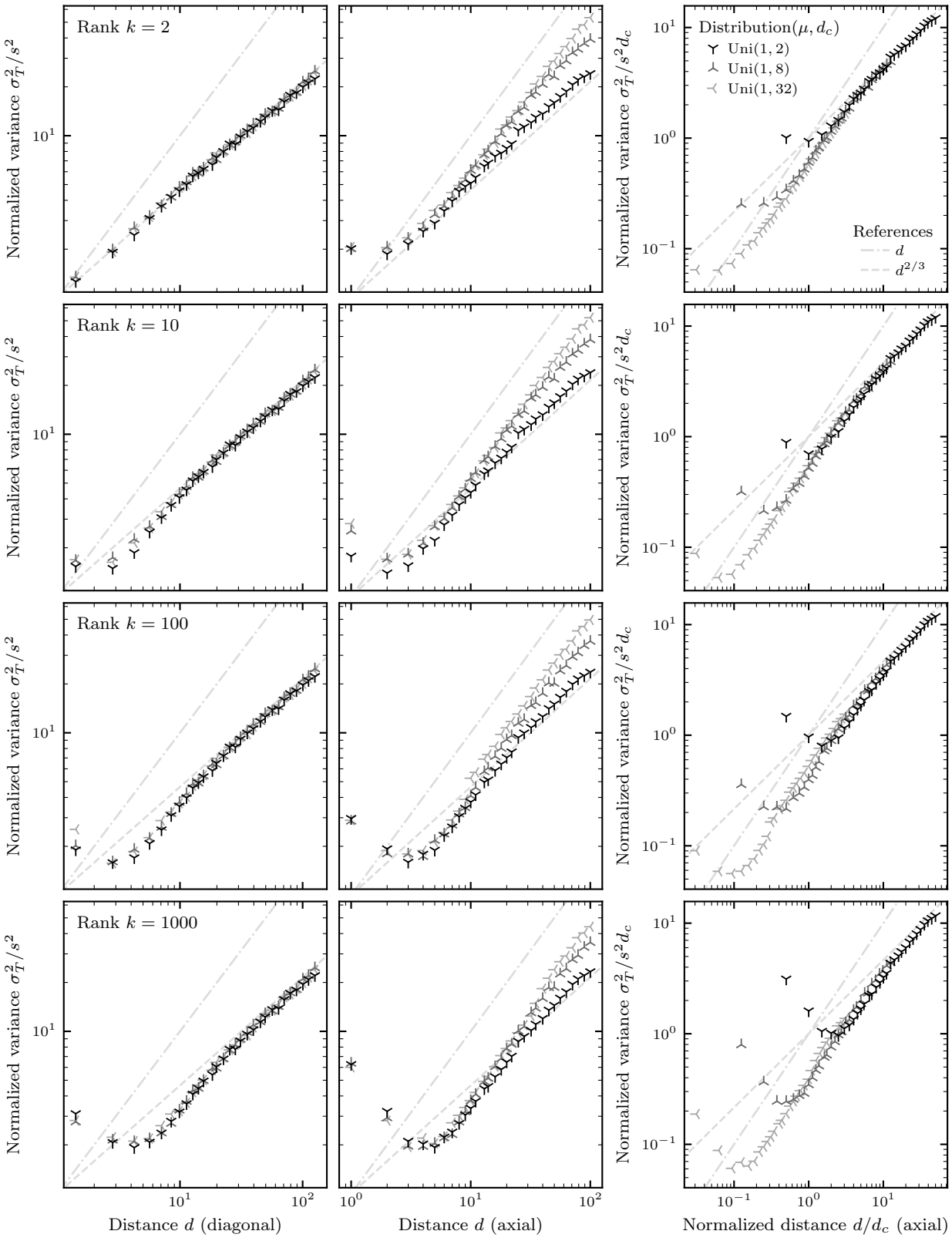

FIG. 16: Same results as those of figure 11 but for $k = 2$, 10, 100 and 1000.

Finally, it is worth noting that the curves for the normalized variables d/d_c, $\sigma_T^2/s^2 d_c$ seem to collapse after their respective transients.

V. CONCLUSIONS AND FUTURE WORK

Visual inspection of individual samples clearly shows hierarchical structures in the ensembles of kSSP, compatible with ultrametricity, with a remarkable resemblance to similar samples in spin-glasses [22, 27–29].

The chief conclusion is that the scaling of the KPP model is linear in the Euclidean distance d from the source when sufficiently ample regions of the kSSP landscape are explored. As the domains narrow, the behaviour gradually reverts to scaling like the FPP model, that is, asymptotically like KPZ. A plausible explanation is that a sufficient amount of averaging will nullify the effect of nucleation events on the interfacial growth, essential to KPZ.
Further work in this direction could be directed towards:

- Better characterizing the duration of the pre-asymptotic regime. The understanding of the present heuristic approach based on the overlap cut-off $q_{\text{cut}} = 0.7$ might be deepened by analyzing the number of clusters it generates.

- Analysing the lateral deviation of the geodesics and the balls of the KPP model, analogous to those defined in §II C.

- Considering other distributions and discrete network types.

It is worth noting that the harshest practical limitation of this approach is that, while it is exact, exploring larger graphs or more realizations of the link-times is computationally highly taxing. More importantly, at a fundamental level, the ensemble of k shortest simple paths obeys no thermodynamic considerations or minimum action principle, and so its physicality is dubious—note that the k shortest paths need not be even local minima in the paths landscape; in analogy with spin glasses, they are not "pure" states.

A potentially fruitful alternative would be to apply a temperature to the model that would allow the application of thermodynamic Monte-Carlo models, such as simulated annealing or parallel tempering, resulting in an ensemble of paths with, perhaps, more physical significance. In particular, a partition function would be available, to which the k shortest simple paths would contribute, whether exactly or averaged. Models similar to FPP

that incorporate a temperature, such as directed polymers in random media (DPRM) [2], might provide guidance in this direction. The aforementioned similarities with spin glass models further suggest a thermodynamic approach. Not only might it allow to characterize local minima in the landscape of paths, it could also grant access to larger system sizes and realizations of the randomness.

Finally, this preliminary exploration might serve as a comparison basis for future efforts.

ACKNOWLEDGMENTS

I acknowledge fruitful conversations with Javier Rodríguez-Laguna, Pedro Córdoba-Torres, Silvia N. Santalla and Elka Radoslavova Koroutcheva, and thank their immense care and patience.

---

[1] G. Parisi, Letters in Mathematical Physics **88**, 255 (2009).

[2] T. Halpin-Healy and Y.-C. Zhang, Physics Reports **254**, 215 (1995).

[3] M. Damron, F. Rassoul-Agha, and T. Seppäläinen, Notices of the AMS **63** (2016).

[4] A. P. Kartun-Giles, M. Barthelemy, and C. P. Dettmann, Physical Review E **100**, 032315 (2019).

[5] P. Córdoba-Torres, S. N. Santalla, R. Cuerno, and J. Rodríguez-Laguna, Journal of Statistical Mechanics: Theory and Experiment **2018**, 063212 (2018).

[6] Y. Khaluf, E. Ferrante, P. Simoens, and C. Huepe, Journal of the Royal Society Interface **14**, 20170662 (2017).

[7] E. Ising, Zeitschrift für Physik **31**, 253 (1925).

[8] L. D. Landau, Nature **138**, 840 (1936).

[9] J. Cardy, *Scaling and Renormalization in Statistical Physics*, Cambridge Lecture Notes in Physics, Vol. 5 (Cambridge University Press, 1996).

[10] H. Nishimori and G. Ortiz, *Elements of Phase Transitions and Critical Phenomena*, Oxford Graduate Texts (Oxford University Press, USA, 2011).

[11] N. Goldenfeld, *Lectures on Phase Transitions and the Renormalization Group*, Frontiers in physics (Westview Press, Advanced Book Program, 1992).

[12] L. P. Kadanoff, Physics Physique Fizika **2**, 263 (1966).

[13] K. G. Wilson, Physical Review B **4**, 3174 (1971).

[14] K. G. Wilson, Physical Review B **4**, 3184 (1971).

[15] K. G. Wilson and M. E. Fisher, Physical Review Letters **28**, 240 (1972).

[16] B. Widom, The Journal of Chemical Physics **43**, 3892 (1965).

[17] B. Widom, The Journal of Chemical Physics **43**, 3898 (1965).

[18] S. Kirkpatrick and D. Sherrington, Physical Review B **17**, 4384 (1978).

[19] F. Guerra and F. L. Toninelli, Communications in Mathematical Physics **230**, 71 (2002).

[20] M. Talagrand, *Spin glasses: A challenge for mathematicians. Cavity and mean field models*, Vol. 46 (Springer Science & Business Media, 2003).

[21] H. Nishimori, *Statistical Physics of Spin Glasses and Information Processing*, International Series of Monographs on Physics (Oxford University Press, USA, 2001).

[22] G. S. Hartnett, E. Parker, and E. Geist, Physical Review E **98**, 022116 (2018).

[23] F. Morone, F. Caltagirone, E. Harrison, and G. Parisi, arXiv preprint arXiv:1409.2722 (2014).

[24] J. R. L. de Almeida and D. J. Thouless, Journal of Physics A: Mathematical and General **11**, 983 (1978).

[25] G. Parisi, Journal of Physics A: Mathematical and General **13**, L115 (1980).

[26] D. Panchenko, Annals of Mathematics , 383 (2013).

[27] E. Domany, G. Hed, M. Palassini, and A. P. Young, Physical Review B **64**, 224406 (2001).

[28] H. G. Katzgraber and A. K. Hartmann, Physical Review Letters **102**, 037207 (2009).

[29] H. G. Katzgraber, T. Jörg, F. Krząkała, and A. K. Hartmann, Physical Review B **86**, 184405 (2012).

[30] G. Ódor, Reviews of Modern Physics **76**, 663 (2004).

[31] P. A. Orrillo, S. N. Santalla, R. Cuerno, L. Vázquez, S. B. Ribotta, L. M. Gassa, F. J. Mompean, R. C. Salvarezza, and M. E. Vela, Scientific Reports **7**, 1 (2017).

[32] M. A. C. Huergo, M. A. Pasquale, P. H. González, A. E. Bolzán, and A. J. Arvia, Physical Review E **85**, 011918 (2012).

[33] P. J. Yunker, T. Still, M. A. Lohr, and A. G. Yodh, Nature **476**, 308 (2011).

[34] K. A. Takeuchi, Physica A: Statistical Mechanics and its Applications **504**, 77 (2018).

[35] K. A. Takeuchi and M. Sano, Journal of Statistical Physics **147**, 853 (2012).

[36] K. A. Takeuchi, M. Sano, T. Sasamoto, and H. Spohn, Scientific Reports **1**, 1 (2011).

[37] S. N. Santalla, J. Rodríguez-Laguna, T. LaGatta, and R. Cuerno, New Journal of Physics **17**, 033018 (2015).

[38] M. Kardar, G. Parisi, and Y.-C. Zhang, Physical Review Letters **56**, 889 (1986).

[39] A. Auffinger, M. Damron, and J. Hanson, *Fifty years of first-passage percolation*, Vol. 68 (American Mathematical Society, 2017).

[40] E. W. Dijkstra, Numerische Mathematik **1**, 269 (1959).

[41] M. E. O'Neill, *PCG: A Family of Simple Fast Space-Efficient Statistically Good Algorithms for Random Number Generation*, Tech. Rep. HMC-CS-2014-0905 (Harvey Mudd College, Claremont, CA, 2014).

[42] B. B. Mandelbrot, in *Fractals and Scaling in Finance* (Springer, 1997) pp. 117–145.

[43] P. E. Hart, N. J. Nilsson, and B. Raphael, IEEE Transactions of Systems Science and Cybernetics **4**, 100 (1968).

[44] W. Hoffman and R. Pavley, Journal of the ACM **6**, 506 (1959).

[45] D. Eppstein, SIAM Journal on Computing **28**, 652 (1998).

[46] J. Y. Yen, Management Science **17**, 712 (1971).

[47] vasilyrud (`https://stackoverflow.com/users/8116864/vasilyrud`), Finding kth-shortest paths?, Stack Overflow (2018), `https://stackoverflow.com/questions/7208720/finding-kth-shortest-paths` (version: 2018-11-28).

[48] E. L. Lawler, Management Science **18**, 401 (1972).

[49] E. Hadjiconstantinou and N. Christofides, Networks: An International Journal **34**, 88 (1999).

[50] M. M. B. Pascoal, Ninth DIMACS Implementation Challenge: Shortest Path Problem (2006).

[51] A. P. Singh and D. P. Singh, Procedia Computer Science **48**, 5 (2015).

[52] N. Katoh, T. Ibaraki, and H. Mine, Networks **12**, 411 (1982).

[53] D. Kurz and P. Mutzel, in *27th International Symposium on Algorithms and Computation (ISAAC 2016)* (Leibniz-Zentrum für Informatik, 2016).

[54] Z. Bar-Joseph, D. K. Gifford, and T. S. Jaakkola, Bioinformatics **17**, S22 (2001).

[55] N. Metropolis, A. W. Rosenbluth, M. N. Rosenbluth, A. H. Teller, and E. Teller, The Journal of Chemical Physics **21**, 1087 (1953).